coatings

MDPI

Article

Effects of W Content on Structural and Mechanical Properties of TaWN Films

Li-Chun Chang [1,2], Chin-Han Tzeng [3] and Yung-I Chen [3,4,*]

[1] Department of Materials Engineering, Ming Chi University of Technology, New Taipei 243303, Taiwan; lcchang@mail.mcut.edu.tw
[2] Center for Plasma and Thin Film Technologies, Ming Chi University of Technology, New Taipei 243303, Taiwan
[3] Department of Optoelectronics and Materials Technology, National Taiwan Ocean University, Keelung 202301, Taiwan; 00688017@email.ntou.edu.tw
[4] Center of Excellence for Ocean Engineering, National Taiwan Ocean University, Keelung 202301, Taiwan
* Correspondence: yichen@mail.ntou.edu.tw

Abstract: In this study, TaWN films were fabricated through co-sputtering. The effects of W addition on the structural variation and mechanical properties of these films were investigated. TaWN films formed face-centered cubic (fcc) solid solutions. With the increase in the W content, the fcc phase varied from TaN-dominant to W_2N-dominant, which was accompanied by a decrease in the lattice constant and alterations in material characteristics, such as the chemical bonding and mechanical properties. The phase change was further correlated with the bonding characteristics of films examined by X-ray photoelectron spectroscopy. The hardness increased from 21.7 GPa for a $Ta_{54}N_{46}$ film to 23.2–31.9 GPa for TaWN films, whereas the Young's modulus increased from 277 GPa for the $Ta_{54}N_{46}$ film to 302–391 GPa for the TaWN films. The enhancement in films' mechanical properties was attributed to the strengthening of the solid solution and the phase change. The wear behavior of the fabricated TaWN films was evaluated using the pin-on-disk test. The $Ta_{17}W_{55}N_{28}$ and $Ta_{36}W_{24}N_{40}$ films exhibited an abrasive wear behavior and low wear rates of 4.9–7.6 $\times$ 10^{-6} mm^3/Nm.

Keywords: mechanical properties; sputtering; wear behavior

Citation: Chang, L.-C.; Tzeng, C.-H.; Chen, Y.-I. Effects of W Content on Structural and Mechanical Properties of TaWN Films. *Coatings* **2022**, *12*, 700. https://doi.org/10.3390/coatings12050700

Academic Editor: Esther Rebollar

Received: 12 April 2022
Accepted: 18 May 2022
Published: 20 May 2022

Publisher's Note: MDPI stays neutral with regard to jurisdictional claims in published maps and institutional affiliations.

Copyright: © 2022 by the authors. Licensee MDPI, Basel, Switzerland. This article is an open access article distributed under the terms and conditions of the Creative Commons Attribution (CC BY) license (https://creativecommons.org/licenses/by/4.0/).

1. Introduction

Surface modifications using thin-film deposition technology are applied to achieve advanced material characteristics, such as superior mechanical properties, chemical stability, and oxidation resistance. Transition-metal nitride films, such as TaN [1,2] and W_2N [3,4], which possess simple metal structures with interstitial N atoms, have been developed for decades. The face-centered cubic (fcc) δ-TaN phase was shown to exhibit a B1 structure, in which all the octahedral interstitial sites of the closed-packed Ta atom arrays were filled with N atoms; however, in the fcc β-W_2N phase, only half of the octahedral interstitial sites of the closed-packed W atom arrays contained N atoms [3]. TaN_x films with a high melting point, good oxidation resistance, superior electrical conductivity, and high chemical stability were employed in hard coatings on cutting tools [5,6], protective coatings for glass molding dies [7], thin-film resistors [8], diffusion barriers for Cu metallization [9], and biocompatible materials [10]. TaN_x films fabricated through sputtering formed multiple equilibrium and metastable phases, and their phase constitutions were affected by the nitrogen fraction in the mixed Ar/N_2 gas and the substrate temperature [1]. With increasing N content, W–N films change from body-centered cubic W to fcc W2N and hexagonal WN phases [11]. Lou et al. [4] reported that fcc W_2N was the predominant W–N compound in WN_x films. Moreover, the sputtered TaN films exhibit a wide range of hardness values (12–40 GPa) [2,12–15]. Ternary nitride films, such as CrAlN [16,17], CrWN [18,19], TaZrN [20], and TaWN [21], were exploited to combine multiple functions for enhancing

the properties of binary nitride films. Moreover, the sputtered ternary nitride films commonly formed a ternary solid solution and crystallized into an fcc B1 structure, such as CrMeN films (Me = Mo, Ti, W, Nb [22], and Ta [23]). Similarly, TaZrN [20], TaHfN [24], and TaWN [21] films formed an fcc phase. By contrast, the sputtered TaMoN films comprised fcc (Ta,Mo)N, hexagonal $(Ta,Mo)_2N$, and orthorhombic $(Ta,Mo)_4N$ phases [25]. In particular, TaWN films were applied as hard coatings [21,26,27] and diffusion barriers for Cu metallization [28,29]. Wei and Shieh [21] reported that the addition of W to TaN films increased the hardness, critical load, and oxidation resistance; the hardness increased from 24 to 29 GPa with increasing W content for the as-deposited TaWN films because of the effects of grain refining and compressive stress. Similar effects were observed for CrWN films [18,30]. In [18], the hardness increased from 19 GPa in CrN films to 24 GPa in CrWN films, accompanied by a decrease in crystal size from 38 to 8 nm. In [30], CrWN films with an fcc structure and a (200) orientation exhibited compressive stress levels of 2.1–3.0 GPa and high hardness values of 21–27 GPa. Yang et al. [26] reported that WTaN films exhibited an fcc solid solution when the nitrogen partial pressure was set at 0.46 Pa and the total pressure ($Ar + N_2$) was kept at 0.7 Pa, and the hardness values ranged from 28 to 38 GPa. The highest hardness value of the aforementioned WTaN films occurred at an atomic ratio (Ta/(W + Ta)) of 0.31. Moreover, the hardness level was enhanced to 41 GPa as the nitrogen partial pressure was increased to 0.5 Pa, which formed a mixture of fcc WTaN and hexagonal W(Ta)N phases with a (Ta/(W + Ta)) ratio of 0.46 [31]. Xu et al. [27] reported that depending on the composition of the films, fcc and hexagonal phases were observed in TaWN films and that the addition of W to TaN films increased the hardness from 25 to 32 GPa because of the strengthening of the solid solution and the decrease in the amount of the hexagonal TaN phase. The addition of W into TaN films varied the chemical bonding in the films, which affected the phase evolution and strengthening mechanism of the fabricated TaWN films. Studying the phase evolution of TaWN films according to their chemical composition is crucial. In this study, the bonding characteristics, phase structure, and mechanical properties of TaWN films were investigated.

2. Materials and Methods

TaWN films were deposited on Si substrates and stainless SUS420 plates by a magnetron co-sputtering apparatus [32]. The chemical composition of the SUS420 plates is Fe—13% Cr—0.33% C—1% Si—1% Mn in wt.% [33]. The hardness of tempered SUS420 was HRC 50. After pumping the chamber to a base pressure of 1.33×10^{-4} Pa, the substrate holder was electrically grounded, heated to 400 °C, and rotated at 30 rpm. The samples prepared on SUS420 plates were used for the wear test, whereas the samples on Si substrates were used for all the other tests. The average surface roughness (R_a) of polished SUS420 plates was 1.92 nm, whereas the R_a value of Si substrate was 0.18 nm. The R_a values were determined by using an atomic force microscope (AFM, Dimension 3100 SPM, Nanoscope IIIa, Veeco, Santa Barbara, CA, USA). The scanning area of each image was 5×5 μm^2 with a scanning rate of 1.0 Hz. The adopted Ta and W targets had a diameter of 50.8 mm. Direct current was applied to the targets. Ta interlayers were coated at 200 W for 10 min under an Ar flow rate of 20 sccm and a working pressure of 0.4 Pa. Ternary TaWN films were co-sputtered for 65 min under Ar and N_2 flow rates of 12 and 8 sccm, respectively. The power applied to the Ta target (P_{Ta}) was set at 250, 200, 100, and 50 W with a voltage of 464, 453, 410, and 414 V, respectively. In the meantime, the power applied to the W target (P_W) was set at 50, 100, 200, and 250 W with a voltage of 378, 411, 451, and 459 V, respectively. The total power of ($P_{Ta} + P_W$) was 300 W. Moreover, Ta–N and W–N binary films were prepared under the application of a power of 250 W for 100 min with a voltage of 472 and 456 V, respectively.

The chemical compositions of the films were analyzed using a field emission electron probe microanalyzer (JXA-iHP200F, JEOL, Akishima, Japan). The thicknesses of the films were examined using a field emission scanning electron microscope (SEM, S4800, Hitachi, Tokyo, Japan). The nanostructures were examined using a transmission electron microscope

(TEM, JEM-2010F, JEOL, Akishima, Japan). The TEM samples with a protective Pt layer were prepared using a focused ion beam system (NX2000, Hitachi, Tokyo, Japan). The phases were identified using an X-ray diffractometer (XRD, X'Pert PRO MPD, PANalytical, Almelo, The Netherlands) with Cu $K\alpha$ radiation under the grazing incident mode with an incidence angle of 1°. The lattice constants, a_0, of each film were evaluated according to the following equation:

$$a = a_0 + K \times \frac{\cos^2\theta}{\sin\theta} \quad (1)$$

where a is the lattice constant for the distinct reflection, K is the constant, and θ is the diffraction angle. The Bragg–Brentano scan (θ–2θ scan) mode was employed to determine the texture coefficients [20] and grain size of the films [34]. The texture coefficient (T_c) was defined as

$$\mathrm{Tc}(hkl) = \frac{I_m(hkl)}{I_0(hkl)}\left[\frac{1}{n}\sum_{n=1}^{n}\frac{I_m(hkl)}{I_0(hkl)}\right]^{-1} \quad (2)$$

where $I_m(hkl)$ is the measured relative intensity of the reflection from the (hkl) plane, $I_0(hkl)$ is the relative intensity from the same plane in a standard reference sample, and n is the total number of reflection peaks from the coating. The grain size was calculated as

$$\mathrm{D} = \frac{0.9\lambda}{\beta\cos\theta_B} \quad (3)$$

where D is the grain size, λ is the X-ray wavelength, β is the full width at half maximum (FWHM) of reflection, and θ_B is the Bragg angle.

The bonding characteristics were analyzed using X-ray photoelectron spectroscopy (XPS; PHI 1600, PHI, Kanagawa, Japan) with a monochromatic Al Kα X-ray beam (energy = 1486.6 eV and power = 44.5 W) operated at 15 kV. The C 1s line of the free surface of the films was observed at 284.60 eV. The C 1s line was calibrated using the Greczynski–Hultman method [35,36]. The work function of the $Ta_{36}W_{24}N_{40}$ film examined through ultraviolet photoelectron spectroscopy (PHI VersaProbe III, ULVAC-PHI, Kanagawa, Japan) was 4.74 eV, which recommended the corrected C 1s energy to be 284.84 eV (=289.58–4.74 eV) and the correction for the binding energy levels in the original XPS analyses to be 0.24 eV (=284.84–284.60 eV) [36]. The splitting energies were 1.91 and 2.18 eV for Ta 4f and W 4f doublets [37], respectively. The peaks were fitted with a mixed Gaussian–Lorentzain function. An Ar+ ion beam of 3 keV was used to sputter the coatings for depth profiling, which sputter etching rate was 8.3 nm/min for SiO_2. XPS analyses were conducted at depths of 16.6, 24.9, 33.2, 41.5, and 49.8 nm after the samples were etched for 2, 3, 4, 5, and 6 min, respectively.

The mechanical properties were measured using a nanoindentation tester (TI-900 Triboindenter, Hysitron, Minneapolis, MN, USA) equipped with a Berkovich diamond probe tip, the rounding radius of the indenter was 200 nm in diameter. Hardness and Young's modulus values were calculated using the Oliver and Pharr method [38]. Because all the films had a thickness of >800 nm, their mechanical properties were evaluated in a constant penetration depth mode with an indentation of 70 nm. The residual stress of the films prepared on Si substrates was determined using the curvature method (Stoney's Equation) [39]. The Si substrate was 20 × 20 × 0.525 mm^3. The wear behavior of the films was studied using the pin-on-disk test under a normal load of 1 N, a sliding speed of 31.4 mm/s, and a wear track diameter of 6 mm. A cemented tungsten carbide (WC–6 wt.% Co) ball with a diameter of 6 mm and a hardness of 14.2 GPa was used as the stationary pin.

3. Results

3.1. Chemical Compositions and Phases

Table 1 lists the chemical compositions and thicknesses of the TaWN films, which are designated as $Ta_yW_zN_{(100-y-z)}$. The deposition rates of $Ta_{54}N_{46}$ and $W_{94}N_6$ films, determined from film thickness and deposition time, were 8.9 and 12.0 nm/min, respectively.

When an additional P_W of 50 W was applied in the preparation of a $Ta_{40}W_{15}N_{45}$ film, the deposition rate increased to 12.5 nm/min from 8.9 nm/min for the $Ta_{54}N_{46}$ film. When the P_{Ta}/P_W ratio was varied, the deposition rate increased to 15.2 nm/min in the fabrication of a $Ta_{36}W_{24}N_{40}$ film and then decreased to 14.4 and 13.6 nm/min in the fabrication of $Ta_{17}W_{55}N_{28}$ and $Ta_8W_{68}N_{24}$ films, respectively. The atomic *N/M* ratios (M: the sum of metal atoms) of the $Ta_{54}N_{46}$, $Ta_{40}W_{15}N_{45}$, $Ta_{36}W_{24}N_{40}$, $Ta_{17}W_{55}N_{28}$, and $Ta_8W_{68}N_{24}$ films were 0.85, 0.83, 0.67, 0.39 and 0.32, respectively. The ideal stoichiometry was not obtained for the transition-metal nitride films [40]. Moreover, the chemical compositions of the $Ta_{54}N_{46}$, $Ta_{40}W_{15}N_{45}$, and $Ta_{36}W_{24}N_{40}$ films exhibited sub-stoichiometric ratios of a B1 structure ($N/M < 1.0$), whereas the chemical compositions of the $Ta_{17}W_{55}N_{28}$ and $Ta_8W_{68}N_{24}$ films exhibited sub-stoichiometric ratios of the W_2N structure ($N/M < 0.5$). Furthermore, the fabricated $W_{94}N_6$ film exhibited an extremely low *N/M* ratio of 0.06 and a high deposition rate of 12.0 nm/min, which implied that the $W_{94}N_6$ film formed a metallic W film comprising trivial N atoms. The deviation to the chemical composition ratio of $N/M = 1$ for the aforementioned TaWN films was enhanced by the low formation enthalpy of W_2N. The standard formation enthalpies for TaN and W_2N at 298 K are −252 [41] and −22 kJ/mol [42], respectively, which results in an inferior affinity between N and W atoms correlated with that between N and Ta atoms. Therefore, the *N/M* ratio decreased with increasing W content. The calculated N content N_{cal} was determined according to the stoichiometric ratios of 1.0 for TaN and 0.5 for W_2N compounds, and the ratio of the measured N content to N_{cal} (N/N_{cal}) was 0.85, 0.95, 0.83, 0.63, 0.57 and 0.13 for $Ta_{54}N_{46}$, $Ta_{40}W_{15}N_{45}$, $Ta_{36}W_{24}N_{40}$, $Ta_{17}W_{55}N_{28}$, $Ta_8W_{68}N_{24}$ and $W_{94}N_6$ films, respectively. All of the TaWN films in this study were deficient in N. Similar observations were reported by Yang et al. [26]. In their study, the composition and crystalline phases of W–Ta–N films varied from W_2N-like to TaN-like when increasing the Ta content.

Table 1. Sputtering parameters, chemical compositions, and thicknesses of the TaWN films.

Sample	Power (W)		Chemical Composition (at.%)				*N/M* [1]	*T* [2]	*I* [3]	*R* [4]
	P_{Ta}	P_W	Ta	W	N	O		(nm)	(nm)	(nm/min)
$Ta_{54}N_{46}$	250	0	52.9 ± 0.7	-	44.8 ± 1.1	2.3 ± 0.7	0.85	894	170	8.9
$Ta_{40}W_{15}N_{45}$	250	50	39.3 ± 3.7	14.9 ± 0.9	45.1 ± 3.2	0.7 ± 1.2	0.83	813	152	12.5
$Ta_{36}W_{24}N_{40}$	200	100	35.7 ± 0.4	23.2 ± 0.8	39.5 ± 0.6	1.6 ± 0.0	0.67	986	157	15.2
$Ta_{17}W_{55}N_{28}$	100	200	16.6 ± 0.0	54.4 ± 0.0	27.4 ± 0.0	1.6 ± 0.0	0.39	939	157	14.4
$Ta_8W_{68}N_{24}$	50	250	7.5 ± 0.0	67.0 ± 0.0	24.0 ± 0.0	1.5 ± 0.0	0.32	885	132	13.6
$W_{94}N_6$	0	250	-	87.9 ± 0.6	5.8 ± 0.3	6.3 ± 0.4	0.06	1203	130	12.0

[1] *N/M*: atomic ratio of N to the sum of metal atoms; [2] *T*: film thickness; [3] *I*: Ta interlayer thickness; [4] *R*: Deposition rate of TaWN film.

Figure 1 shows a typical cross-sectional SEM (XSEM) image of TaWN films with a columnar structure. Figure 2a displays the cross-sectional TEM (XTEM) image of the $Ta_{40}W_{15}N_{45}$ sample with a Ta interlayer fabricated on a Si substrate. The inset in Figure 2a shows the selected area electron diffraction (SAED) pattern of the aforementioned sample, which indicates the existence of an fcc phase with evident (111), (200), (220) and (311) diffraction rings. The (111) and (200) diffraction rings had *d*-spacings of 0.250 and 0.217 nm, respectively, which are comparable with the standard values (0.2504 and 0.2169 nm) for the fcc TaN phase (ICDD 00-049-1283). Figure 2b,c depict the dark-field images corresponding to the (111) and (200) diffraction spots shown in Figure 2a, respectively. Columnar structures with widths of 24–45 and 25–51 nm existed in the aforementioned dark-field images, respectively. Lattice fringes of 0.251 and 0.217 nm corresponding to the (111) and (200) planes of the fcc TaN phase, respectively, were observed in the high-resolution TEM (HRTEM) image of the aforementioned sample (Figure 2d). The XTEM image and SAED pattern of the $Ta_{17}W_{55}N_{28}$ sample (Figure 3a) were similar to those of the $Ta_{40}W_{15}N_{45}$ sample. The dark-field image corresponding to the (111) diffraction spot of the $Ta_{17}W_{55}N_{28}$ sample exhibited columnar widths of 36–81 nm (Figure 3b), which were larger than those

of the $Ta_{40}W_{15}N_{45}$ sample. The HRTEM image of the $Ta_{17}W_{55}N_{28}$ film (Figure 3c) exhibited lattice fringes of TaN and W_2N crystallites.

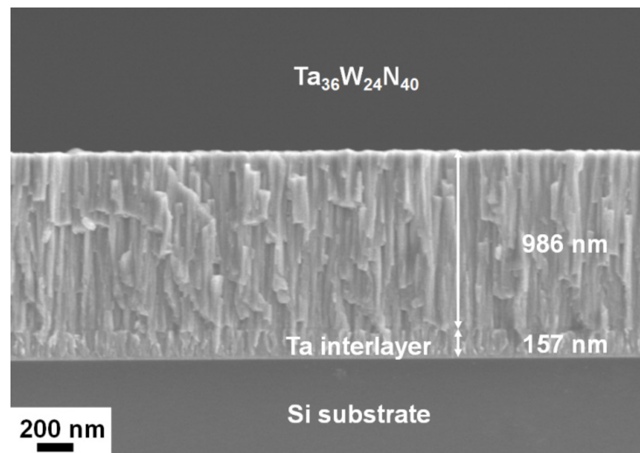

Figure 1. XSEM image of the $Ta_{36}W_{24}N_{40}$ film prepared on a Si substrate.

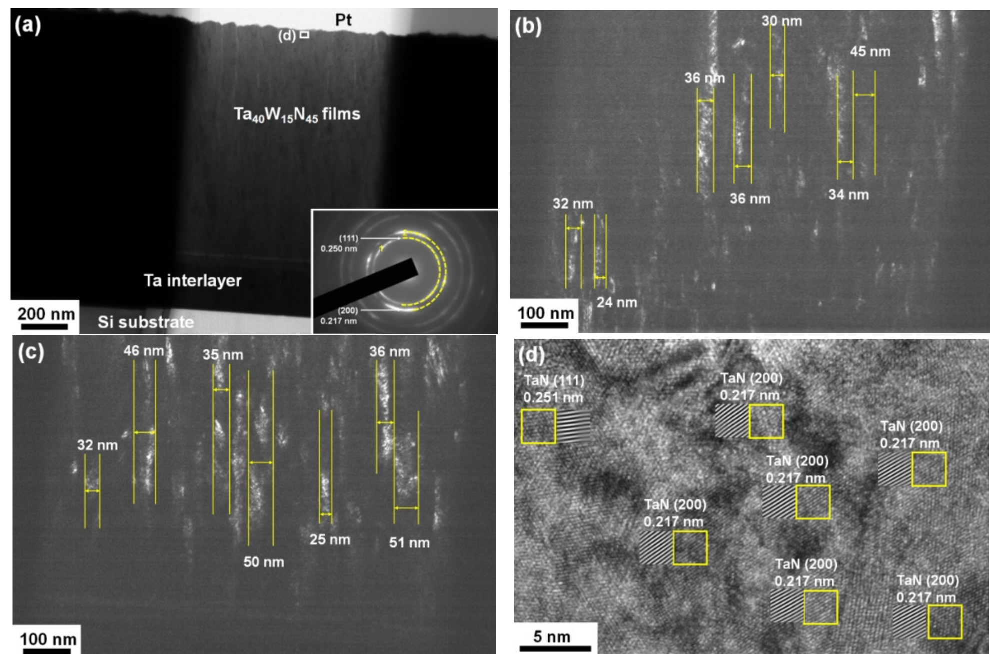

Figure 2. (**a**) XTEM image and SAED pattern, dark-field images corresponding to the (**b**) (111) and (**c**) (200) spots in SAED pattern and (**d**) HRTEM image of the $Ta_{40}W_{15}N_{45}$ film.

Figure 4 exhibits the grazing incident XRD (GIXRD) patterns of the TaWN films. The $Ta_{54}N_{46}$, $Ta_{40}W_{15}N_{45}$, and $Ta_{36}W_{24}N_{40}$ films exhibited an fcc phase with reflections close to the standard reflection angles of fcc TaN, whereas the reflections of the $Ta_{17}W_{55}N_{28}$ and $Ta_8W_{68}N_{24}$ films were located between the standard reflection angles of the TaN and W_2N phases. The vertical lines in Figure 4 indicate the standard positions of reflections for TaN and W_2N phases. Figure 5 illustrates the lattice constants of the TaWN films determined using (111), (200), (220), and (311) reflections in the GIXRD patterns. The standard lattice constant values of TaN (0.43399 nm) and W_2N (0.41260 nm) are also shown for comparison. The atomic radii of Ta and W are 0.1430 and 0.1367 nm [43], respectively, which implies that substituting W atoms into the TaN lattice should decrease the lattice constant. The addition of W to the TaN lattice decreased the lattice constant from 0.4365 nm for the $Ta_{54}N_{46}$ film to 0.4342 and 0.4335 nm for the $Ta_{40}W_{15}N_{45}$ and $Ta_{36}W_{24}N_{40}$ films, respectively; then, the decrease in lattice constant became more evident, being reduced to 0.4242 and 0.4207 nm for

the $Ta_{17}W_{55}N_{28}$ and $Ta_8W_{68}N_{24}$ films, respectively. Two linear fitting lines were obtained for the groups of (1) $Ta_{54}N_{46}$, $Ta_{40}W_{15}N_{45}$, and $Ta_{36}W_{24}N_{40}$ films and (2) $Ta_{17}W_{55}N_{28}$ and $Ta_8W_{68}N_{24}$ films and the standard W_2N, respectively. The variation in the tendency to decrease with increasing W content implied the formation of solid solutions accompanied by the phase change from TaN-dominant to W_2N-dominant structures. This observation is different from that reported by Yang et al. [26]. In their study [26], the lattice constant of W–Ta–N films linearly increased with increasing Ta content in the entire concentration range. The $W_{94}N_6$ films exhibited a body-centered cubic W phase with a lattice constant of 0.3160 nm determined from (110), (200), and (211) reflections. The standard lattice constant of cubic W is 0.31648 nm (ICDD 00-004-0806).

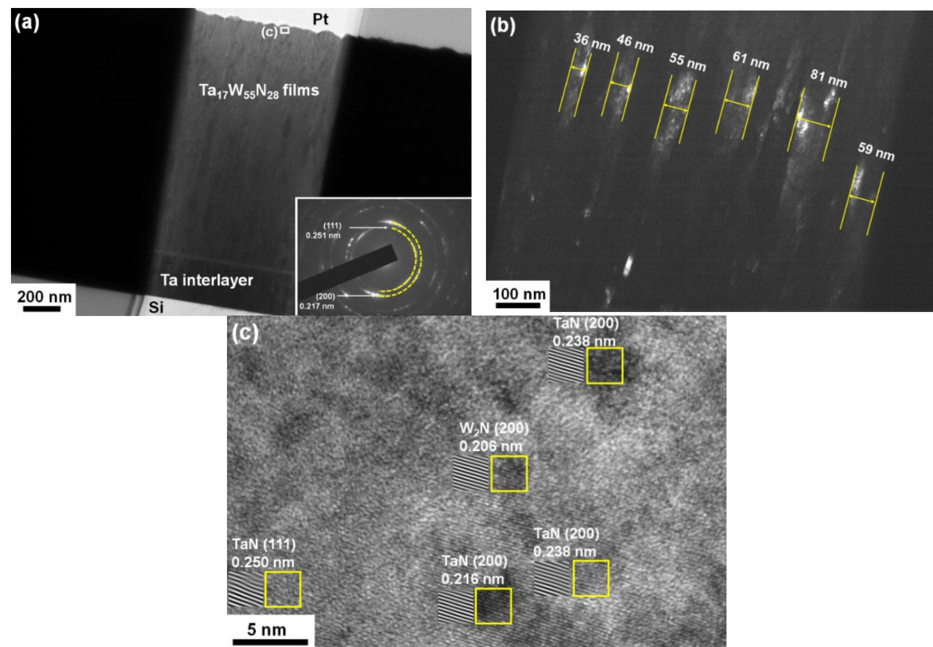

Figure 3. (**a**) XTEM image and SAED pattern, (**b**) dark-field image corresponding to the (200) spot in the SAED pattern, and (**c**) HRTEM image of the $Ta_{17}W_{55}N_{28}$ film.

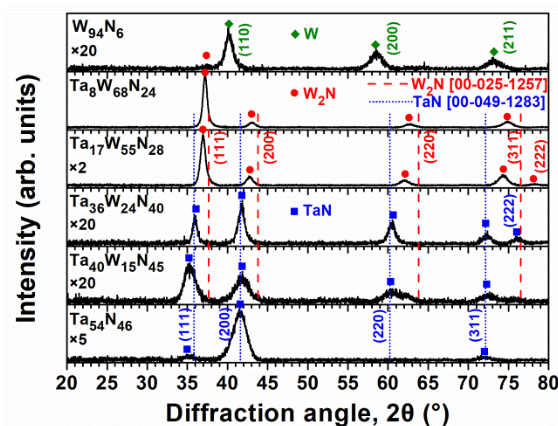

Figure 4. GIXRD patterns of the TaWN films. (Vertical lines indicate the standard positions of reflections for TaN (ICDD 00-049-1283) and W_2N (ICDD 00-025-1257), respectively).

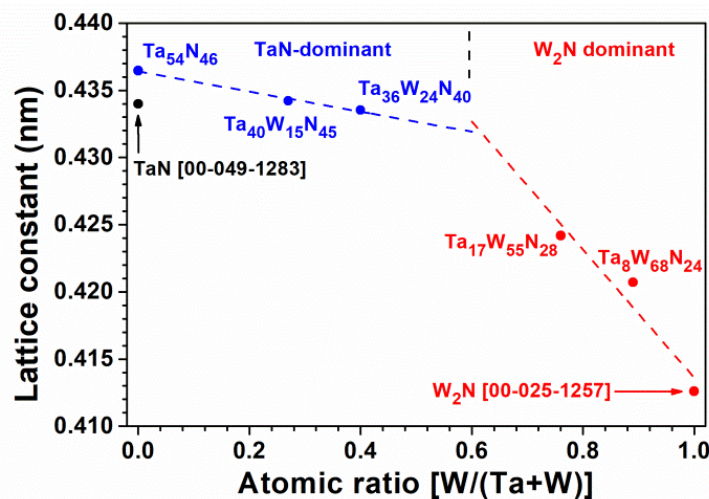

Figure 5. Lattice constants of the TaWN films.

3.2. Chemical Bonding

Figure 6 displays the XPS analyses of TaWN films at a depth of 49.8 nm. Ta 4*f*, W 4*f*, and N 1*s* signals were recorded. The aforementioned formation enthalpy for TaN and W_2N at 298 K implied that TaN should have formed first, followed by W_2N. Because all of the TaWN films were N-deficient, the Ta signals comprised two 4*f* doublets contributed by Ta–N bonds in Ta_2N and TaN. The intensity ratios of Ta–N bonds of Ta_2N to that of TaN (I_{Ta2N}:I_{TaN}) were in the range of 24:76 to 33:67, as shown in Table 2. Table 2 lists the XPS analysis results obtained for the TaWN films at depths of 16.6, 24.9, 33.2, 41.5 and 49.8 nm. The binding energy values of Ta $4f_{7/2}$ for the Ta–N bonds in Ta_2N and TaN compounds in the aforementioned TaWN films were 22.47–22.75 and 23.07–23.32 eV, respectively, which were comparable to the reported binding energies of Ta $4f_{7/2}$ of 22.3–22.9 eV [44–47] for Ta–N bonds in Ta_2N and Ta $4f_{7/2}$ of 23.0–23.7 eV [44–48] for Ta–N bonds in TaN, respectively. The Ta $4f_{7/2}$ value for Ta–Ta bonds in pure Ta was 21.7–21.9 eV in the literature [44,45,47], which was not observed in this study. The $4f_{7/2}$ levels for pure Ta and W were 21.9 and 31.4 eV [37], respectively, and the standard values for 4*f* doublets were marked in Figure 6 for comparison. The W signals comprised W–W and W–N 4*f* doublets and a minor W–W $5p_{3/2}$ component and W–W bonds were the major forms of bonding. The intensity ratio I_{W-W}:I_{W-N} was higher than 68:32 for all the W-contained films. The low intensity of W–N bonds indicated the low affinity between W and N atoms. The binding energy values of W $4f_{7/2}$ for the W–W and W–N bonds in the fabricated TaWN films were 31.17–31.44 and 32.27–33.05 eV, respectively, which were comparable to the reported 31.2–31.7 eV for W films and 32.1–33.1 eV for W–N bonds [49–52]. The N 1*s* signals comprised N–Ta, N–W, and Ta $4p_{3/2}$ components. The N 1*s* signal of the $Ta_{54}N_{46}$ and $W_{94}N_6$ films was 397.44 and 397.71 eV, respectively. Moreover, the binding energy values of N–Ta and N–W bonds in the fabricated TaWN films were 397.27–397.41 and 397.83–397.95 eV, respectively, which implied that the N 1*s* binding energy levels of the N–W bonds were higher than those of the N–Ta bonds. Shen and Wang [53] reported that the binding energy values of N 1*s* were 396.9 and 397.9 eV in TaN and W_2N, respectively. Greczynski et al. [54] reported 397.54 and 397.94 eV for the N 1*s* binding energy values of TaN and WN films, respectively. By contrast, Yang et al. [26] reported 397.3 and 398 eV for N–W and N–Ta binding energies, respectively.

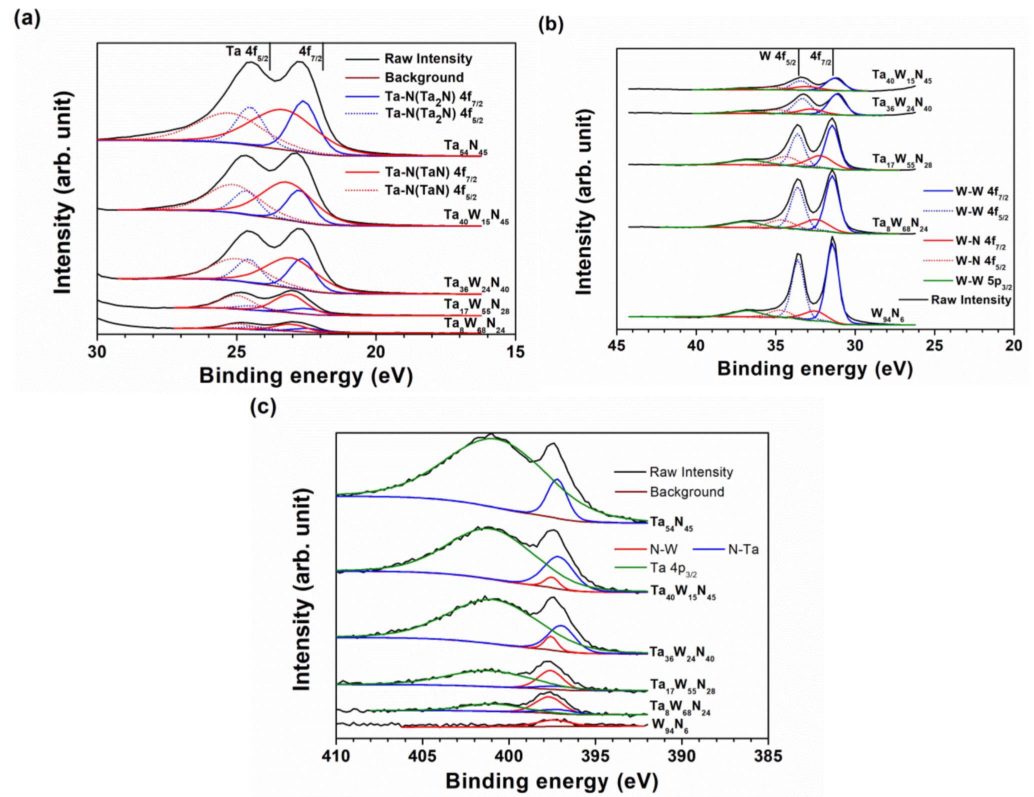

Figure 6. (**a**) Ta, (**b**) W, and (**c**) N signals at a depth of 49.8 nm for the TaWN films.

Table 2. XPS analysis results for the TaWN films at depths of 16.6–49.8 nm.

Sample	Ta $4f_{7/2}$ (eV)		I_{Ta2N}:I_{TaN} [1]	W $4f_{7/2}$ (eV)		$I_{W–W}$:$I_{W–N}$ [2]	N 1*s* (eV)		$I_{N–Ta}$:$I_{N–W}$ [3]
	$(Ta–N)_{Ta2N}$	$(Ta–N)_{TaN}$		W–W	W–N		N–Ta	N–W	
$Ta_{54}N_{46}$	22.60 ± 0.01	23.32 ± 0.01	33:67	-	-	-	397.44 ± 0.01	-	100:0
$Ta_{40}W_{15}N_{45}$	22.75 ± 0.01	23.22 ± 0.02	28:72	31.29 ± 0.02	33.05 ± 0.06	68:32	397.31 ± 0.04	397.85 ± 0.05	80:20
$Ta_{36}W_{24}N_{40}$	22.66 ± 0.01	23.07 ± 0.02	32:68	31.17 ± 0.02	32.76 ± 0.13	73:27	397.27 ± 0.04	397.83 ± 0.06	82:18
$Ta_{17}W_{55}N_{28}$	22.52 ± 0.04	23.10 ± 0.01	24:76	31.44 ± 0.00	32.27 ± 0.07	68:32	397.33 ± 0.05	397.87 ± 0.02	26:74
$Ta_8W_{68}N_{24}$	22.47 ± 0.04	23.07 ± 0.02	30:70	31.43 ± 0.01	32.40 ± 0.13	72:28	397.41 ± 0.04	397.95 ± 0.03	26:74
$W_{94}N_6$	-	-	-	31.43 ± 0.01	32.58 ± 0.03	82:18	-	397.71 ± 0.13	0:100

[1] I_{Ta2N}:I_{TaN}: intensity ratio of Ta–N bonds in the Ta_2N phase to those in the TaN phase; [2,3] $I_{X–Y}$: intensity of X–Y bonds.

3.3. Mechanical Properties

Table 3 lists the mechanical properties of the TaWN films. The average surface roughness values of TaWN films prepared on Si substrates were in the range of 1.6–2.7 nm, except for the $W_{94}N_6$ films, with a higher value of 4.7 nm, whereas the aforementioned films fabricated on the SUS420 plates revealed higher R_a values of 2.7–6.4 nm; however, all these R_a values were far below the radius of the probe tip used for nanoindentation testing. The $Ta_{54}N_{46}$ film exhibited a hardness (H) of 21.7 GPa and a Young's modulus (E) of 277 GPa. The mechanical properties of the transition-metal nitride films were influenced by chemical stoichiometry, grain size, phase constitution, crystalline orientation, and residual stress caused by the formation technique. Various equilibrium and metastable phases of TaN films were studied [1]. In the present study, the TaWN films formed fcc solid solutions in which the lattice structures were TaN- or W_2N-dominant depending on the chemical composition. With the addition of W to TaN, the hardness value increased from 21.7 GPa for the $Ta_{54}N_{46}$ film to 23.2, 24.5, 29.9, and 31.9 GPa for the $Ta_{40}W_{15}N_{45}$, $Ta_{36}W_{24}N_{40}$, $Ta_{17}W_{55}N_{28}$ and $Ta_8W_{68}N_{24}$ films, respectively, whereas the Young's modulus value increased from 277 GPa for the $Ta_{54}N_{46}$ film to 302, 351, 381 and 391 GPa for the $Ta_{40}W_{15}N_{45}$, $Ta_{36}W_{24}N_{40}$, $Ta_{17}W_{55}N_{28}$ and $Ta_8W_{68}N_{24}$ films, respectively. By contrast, in [20], the hardness of TaZrN films decreased with increasing Zr content. The hardness

decreased from 29.4 GPa for $TaN_{0.86}$ film to 27.3, 26.3, 22.0 and 15.9 GPa for $Ta_{0.95}Zr_{0.05}N_{0.97}$, $Ta_{0.59}Zr_{0.41}N_{1.09}$, $Ta_{0.28}Zr_{0.72}N_{1.05}$ and $ZrN_{1.00}$ films, respectively [20]. The atomic radius of Zr is 0.16025 nm [43], which is larger than that of Ta (0.1430 nm) and W (0.1367 nm); therefore, the addition of Zr into the TaN matrix contributed a tensile stress component to the TaZrN solid solution, which resulted in variation in the residual stress from −3.46 GPa for $TaN_{0.86}$ film to −2.62, −1.77, −0.01 and −0.11 GPa for the $Ta_{0.95}Zr_{0.05}N_{0.97}$, $Ta_{0.59}Zr_{0.41}N_{1.09}$, $Ta_{0.28}Zr_{0.72}N_{1.05}$ and $ZrN_{1.00}$ films [20]. The addition of W into the TaN matrix should increase the compressive stress level if the TaWN films formed a solid solution. However, all the TaWN films except for the $Ta_{17}W_{55}N_{28}$ film exhibited a compressive residual stress level of 1.6–1.7 GPa. The $Ta_{17}W_{55}N_{28}$ sample exhibited marginally high stress of −2.5 GPa; however, the hardness of the $Ta_{17}W_{55}N_{28}$ sample (29.9 GPa) was lower than that of the $Ta_8W_{68}N_{24}$ sample (31.9 GPa). The deviation in the hardness for the aforementioned TaWN films was not dominated by residual stress.

Table 3. Mechanical properties of the TaWN/Ta/Si samples.

Sample	*H* [1]	*E* [2]	*H*/*E*	*H*/*E** [3]	H^3/E^2	W_e [4]	σ [5]	R_a [6]
	(GPa)	(GPa)				(%)	(GPa)	(nm)
$Ta_{54}N_{46}$	21.7 ± 2.5	277 ± 22	0.078	0.069	0.133	59	−1.6 ± 0.1	2.6
$Ta_{40}W_{15}N_{45}$	23.2 ± 1.1	302 ± 7	0.077	0.068	0.137	60	−1.7 ± 0.2	2.1
$Ta_{36}W_{24}N_{40}$	24.5 ± 1.7	351 ± 25	0.070	0.062	0.119	59	−1.7 ± 0.0	2.7
$Ta_{17}W_{55}N_{28}$	29.9 ± 0.8	381 ± 12	0.078	0.071	0.184	63	−2.5 ± 0.1	1.6
$Ta_8W_{68}N_{24}$	31.9 ± 1.9	391 ± 18	0.082	0.074	0.212	61	−1.7 ± 0.2	2.5
$W_{94}N_6$	23.0 ± 3.4	315 ± 31	0.073	0.067	0.123	55	−0.7 ± 0.1	4.7

[1] *H*: hardness; [2] *E*: Young's modulus; [3] *E**: effective Young's modulus; [4] W_e: elastic recovery; [5] σ: residual stress; [6] R_a: average surface roughness.

Yang et al. [26] and Xu et al. [27] reported that the hardness of TaWN films initially increased and then decreased with increasing W content. Yang et al. [26] observed a maximal hardness of 38 GPa for a $Ta_{17}W_{38}N_{45}$ film because of the strengthening of the solid solution and the preferred (200) orientation, and Xu et al. [27] observed a maximal hardness of 32 GPa for a $Ta_{41}W_{17}N_{42}$ film because of the strengthening of the solid solution and the phase change. Figure 7 displays the Bragg–Brentano XRD patterns of the TaWN films in this study. The reflections from the Ta interlayer and Si substrate were also observed. The TaN-dominant $Ta_{54}N_{46}$, $Ta_{40}W_{15}N_{45}$ and $Ta_{36}W_{24}N_{40}$ films exhibited high (200) intensities, whereas the W_2N-dominant $Ta_{17}W_{55}N_{28}$ and $Ta_8W_{68}N_{24}$ films exhibited both (111) and (200) reflections. The grain sizes determined from the FWHM of (200) reflections in the Bragg–Brentano XRD patterns were 3.6, 3.7, 7.8, 15.6 and 12.0 nm for the $Ta_{54}N_{46}$, $Ta_{40}W_{15}N_{45}$, $Ta_{36}W_{24}N_{40}$, $Ta_{17}W_{55}N_{28}$ and $Ta_8W_{68}N_{24}$ films, respectively. The increase in the grain size of the aforementioned TaWN films was accompanied by an increase in hardness, which exhibited the inverse Hall–Petch relationship [55,56]. The Hall–Petch strengthening mechanism, which originated from the dislocation pile-up model, demonstrates the hardness enhancement with decreasing grain sizes for polycrystalline materials. Further decreasing the grain size to below a critical size such as 30 nm for nanocrystalline materials resulted in an inverse Hall–Petch behavior because of grain size softening effects, such as grain sliding or rotation. The critical grain size was reported to be 10, 12 and 10 nm for TaN [14], CrN [57] and TiZrN [58] films, respectively. In this study, the critical size was approximately 12 nm. The grain sizes of TaWN films reported in the works of Yang et al. [26] and Xu et al. [27] exhibited wider and higher ranges of 9–28 and 11–19 nm, respectively. The low intensity of the W(110) reflection in the Bragg–Brentano XRD pattern of the $W_{94}N_6$ films related to that shown in the GIXRD pattern was attributed to the effect of texture.

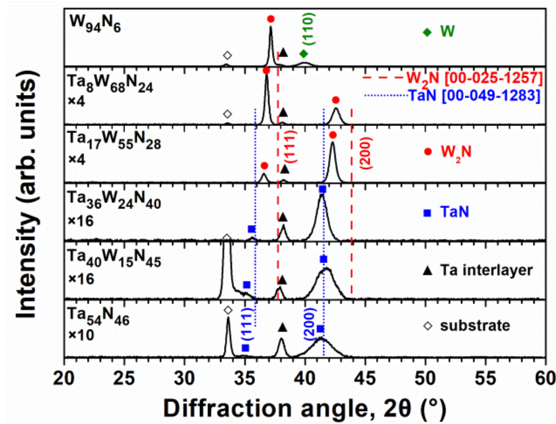

Figure 7. Bragg–Brentano XRD patterns of the TaWN films.

Figure 8 shows the texture coefficients of TaWN films, which indicates a (200) orientation for the reflections of all the TaWN films. The texture coefficients of the $Ta_{40}W_{15}N_{45}$ and $Ta_{36}W_{24}N_{40}$ films were determined using the standard value of 100:68 for the (111):(200) intensity ratio of the fcc TaN phase (ICDD 00-049-1283), whereas the texture coefficients of the $Ta_{17}W_{55}N_{28}$ and $Ta_{8}W_{68}N_{24}$ films were calculated using the standard value of 100:47 for the (111):(200) intensity ratio of the fcc W_2N phase (ICDD 00-025-1257). The T_c(111):T_c(200) ratios exhibited similar levels of 0.05:1.95 and 0.08:1.92 for the $Ta_{40}W_{15}N_{45}$ and $Ta_{36}W_{24}N_{40}$ films, respectively, and changed to 0.16:1.84 and 0.71:1.29 for the W_2N-dominant $Ta_{17}W_{55}N_{28}$ and $Ta_{8}W_{68}N_{24}$ films, respectively. The TaN film exhibited (200) texture because it possessed the lowest surface energy in a NaCl structure [59], whereas (111) planes were the closest packed in the fcc W_2N structure with the lowest surface energy [60]. Therefore, the T_c (111) value increased with increasing W content in the TaWN films.

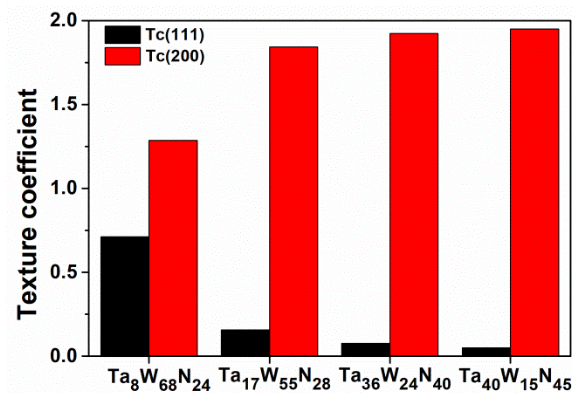

Figure 8. Texture coefficients of the TaWN films.

In a previous study [61], a $W_{77}N_{23}$ film that was prepared under a P_W value of 150 W and a nitrogen flow ratio $[N_2/(N_2 + Ar)]$ of 0.4 at room temperature exhibited a W_2N phase, a residual stress of −1.6 GPa, a hardness of 25.9 GPa, and a Young's modulus of 347 GPa. Under a stress level of −1.6 GPa, the hardness values of the $Ta_{54}N_{46}$ and $W_{77}N_{23}$ films were 21.7 and 25.9 GPa, respectively. Figure 9 depicts the relationship between the hardness values and atomic ratio (W/(Ta + W)) of the TaWN films. All TaWN films exhibited hardness levels above the line combining the hardness values of $Ta_{54}N_{46}$ and $W_{77}N_{23}$ films. This result implies that strengthening the solid solution and phase variation from TaN- to W_2N-dominance are the main factors affecting the mechanical properties of TaWN films.

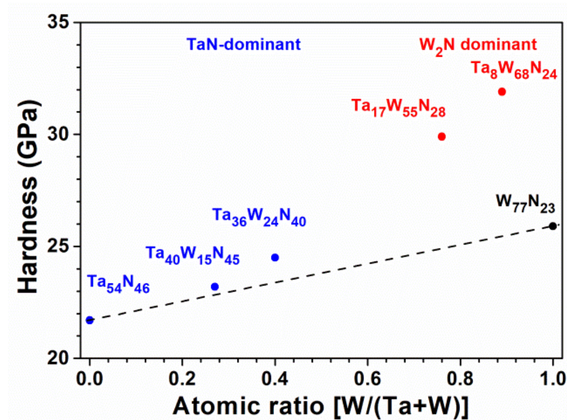

Figure 9. Hardness values of the TaWN films.

The indicators H/E, H/E^* (E^*: effective Young's modulus), *We* (elastic recovery), and H^3/E^2 were used to evaluate the toughness and wear behavior of the fabricated films [62–64]. However, the use of H/E and H^3/E^2 to indicate the coating toughness of plastic materials was criticized [65]. In this study, the fcc TaWN films exhibited similar H/E values of 0.070–0.082, H/E* values of 0.062–0.074, and *We* values of 59–63% (Table 3), which implied that these films exhibited similar toughness. However, the H^3/E^2 values varied over a wide range, from 0.119 to 0.212 GPa (Table 3). $Ta_{36}W_{24}N_{40}$ films exhibited the lowest levels of the aforementioned indicators within these fcc TaWN films. Figure 10 shows the wear scars of the TaWN/Ta/SUS420 samples against cemented tungsten carbide balls. The TaN-dominant $Ta_{54}N_{46}$, $Ta_{40}W_{15}N_{45}$ and $Ta_{36}W_{24}N_{40}$ films exhibited distinct morphologies after the wear test. The $Ta_{54}N_{46}$/Ta/SUS420 sample exhibited adhesive wear because of the chemical reaction on the contact area between the counterpart ball and films [59,66]. The wear debris attached to the films. The wear track width was 130–152 µm. The $Ta_{40}W_{15}N_{45}$/Ta/SUS420 sample exhibited a wear track width of 166 µm. Crack propagation and peeling-off were observed in the inner part of the wear track. Figure 11 depicts the SEM image and elemental mappings of the $Ta_{40}W_{15}N_{45}$/Ta/SUS420 sample, which exhibits an exposed substrate after the wear test. Fe and Cr signals attributed to the SUS420 substrate were observed at the interior of the wear track, whereas Ta, W, and N signals were absent. The peeling-off part of the $Ta_{40}W_{15}N_{45}$ film revealed enriched Ta, W and O signals, but was N-deficient. The wear track of the $Ta_{36}W_{24}N_{40}$/Ta/SUS420 sample was smooth and flat, which represented an abrasive wear behavior [66]. Table 4 lists the wear test results. The $Ta_{54}N_{46}$/Ta/SUS420 sample exhibited a wear depth of 682 nm, a coefficient of friction (COF) of 0.41, and a wear rate of 1.4×10^{-5} mm^3/Nm. The addition of W into the TaN-dominant films increased the COFs to 0.77–0.78, whereas the wear rate was decreased to 8.3 and 7.6×10^{-6} mm^3/Nm for the $Ta_{40}W_{15}N_{45}$ and $Ta_{36}W_{24}N_{40}$ samples, respectively. The W_2N-dominant TaWN films, namely the $Ta_{17}W_{55}N_{28}$ and $Ta_8W_{68}N_{24}$ films, exhibited higher H^3/E^2 levels than those of the other films, which implied that the $Ta_8W_{68}N_{24}$ film should have high wear resistance. However, the $Ta_8W_{68}N_{24}$/Ta/SUS420 sample exhibited the most severe wear damage (Figure 10), with a wear depth of 1404 nm, which was greater than the sum of this sample's film and interlayer thicknesses (1017 nm). Figure 12 displays the variations in the coefficient of friction (COF) values of the TaWN/Ta/SUS420 samples after sliding for 50 m. The $Ta_8W_{68}N_{24}$/Ta/SUS420 sample exhibited abrupt deviations after sliding for 40 m. The low wear resistance of the $Ta_8W_{68}N_{24}$/Ta/SUS420 sample could be attributed to the film's texture, containing both (111) and (200) orientations. A TaN film with (111) texture was proposed to achieve adhesive wear behavior [59]. Samples with $Ta_{36}W_{24}N_{40}$ and $Ta_{17}W_{55}N_{28}$ top layers exhibited smooth wear scars, and their wear depths were smaller than their film thicknesses. The wear rates of the $Ta_{36}W_{24}N_{40}$ and $Ta_{17}W_{55}N_{28}$ samples were 7.6 and 4.9×10^{-6} mm^3/Nm, respectively. The sample with a $W_{94}N_6$ top layer also exhibited a smooth wear scar and the lowest wear rate of 2.6×10^{-6} mm^3/Nm because of its metallic W phase. The wear rate of the

abrasive-wear-type samples decreased from 7.6 to 4.9 and 2.6 × 10^{-6} mm^3/Nm as the COF value decreased from 0.77 to 0.74 and 0.40.

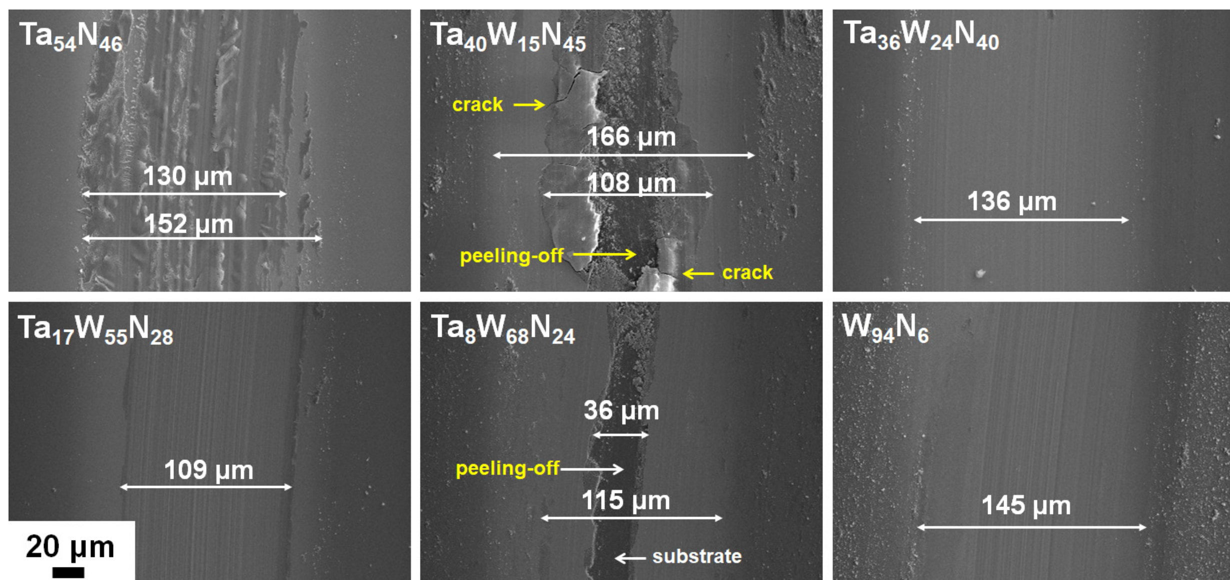

Figure 10. Wear scars of the TaWN/Ta/SUS420 samples after sliding for 50 m.

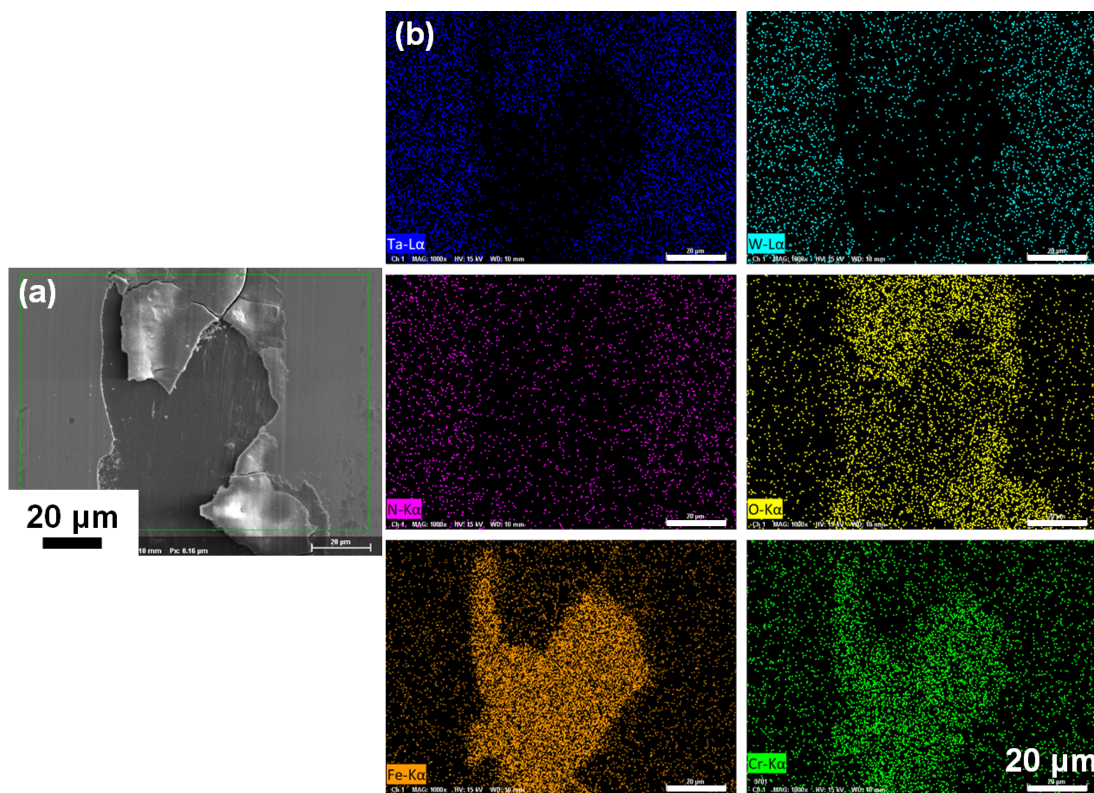

Figure 11. (**a**) SEM image and (**b**) elemental mappings of the $Ta_{40}W_{15}N_{45}$ film after the wear test.

Table 4. Wear test results for the TaWN/Ta/SUS420 samples.

Sample	Thickness	Wear Depth	μ [1]	Wear Rate	R_a [2]	H^3/E^2
	(nm)	(nm)		(mm^3/Nm)	(nm)	(GPa)
$Ta_{54}N_{46}$	894	682	0.41	1.4×10^{-5}	3.1	0.133
$Ta_{40}W_{15}N_{45}$	813	1224	0.78	8.3×10^{-6}	2.7	0.137
$Ta_{36}W_{24}N_{40}$	986	322	0.77	7.6×10^{-6}	2.9	0.119
$Ta_{17}W_{55}N_{28}$	939	251	0.74	4.9×10^{-6}	3.1	0.184
$Ta_8W_{68}N_{24}$	885	1404	0.59	2.7×10^{-5}	4.2	0.212
$W_{94}N_6$	1203	200	0.40	2.6×10^{-6}	6.4	0.123

[1] μ: coefficient of friction; [2] R_a: average surface roughness.

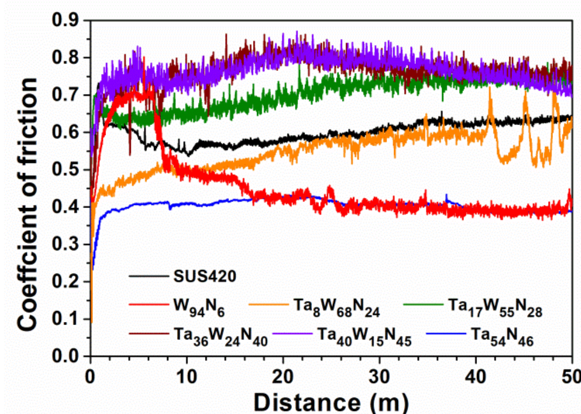

Figure 12. COFs of the TaWN/Ta/SUS420 samples.

4. Conclusions

In this study, TaWN films with a Ta interlayer were fabricated using the direct current magnetron co-sputtering technique. The fabricated ternary TaWN films exhibited fcc solid solutions. Their structure changed from being TaN-dominant to being W_2N-dominant when their W content was increased. Moreover, the chemical compositions of the aforementioned films exhibited sub-stoichiometric ratios in their fcc structures because of the low affinity between N and W atoms. The mechanical properties of the TaWN films improved when their W content was increased, which was attributed to the strengthening of the solid solution and the phase change from a TaN-dominant fcc to a W_2N-dominant fcc. The $Ta_8W_{68}N_{24}$ film exhibited the highest hardness (31.9 GPa) and Young's modulus (391 GPa) as well as a low wear resistance in the pin-on-disk test. The $Ta_{17}W_{55}N_{28}$ film exhibited the following acceptable mechanical properties: a hardness of 29.9 GPa, a Young's modulus of 381 GPa, and a low wear rate of 4.9×10^{-6} mm^3/Nm.

Author Contributions: Conceptualization, L.-C.C. and Y.-I.C.; Funding acquisition, L.-C.C. and Y.-I.C.; Investigation, C.-H.T.; Resources, L.-C.C. and Y.-I.C.; Validation, L.-C.C.; Visualization, C.-H.T.; Writing—original draft, C.-H.T.; Writing—review and editing, Y.-I.C. All authors have read and agreed to the published version of the manuscript.

Funding: This research was funded by the Ministry of Science and Technology, Taiwan, grant numbers 110-2221-E-019-015 and 110-2221-E-131-013. The APC was funded by the National Taiwan Ocean University.

Institutional Review Board Statement: Not applicable.

Informed Consent Statement: Not applicable.

Data Availability Statement: Not applicable.

Acknowledgments: The authors thank the Instrumentation Center at the National Tsing Hua University for EPMA and XPS analyses (MOST 110-2731-M-007-001, EPMA000200 and ESCA000300). Thanks are also given to the Joint Center for High Valued Instruments at NSYSU for the FIB (EM025100) operation.

Conflicts of Interest: The authors declare no conflict of interest.

References

1. Shin, C.S.; Kim, Y.W.; Gall, D.; Greene, J.E.; Petrov, I. Phase composition and microstructure of polycrystalline and epitaxial TaN_xlayers grown on oxidized Si(001) and MgO(001) by reactive magnetron sputter deposition. *Thin Solid Films* **2002**, *402*, 172–182. [CrossRef]
2. Li, H.; Li, J.; Yan, C.; Huang, J.; Kong, J.; Wu, Q.; Shi, Y.; Xiong, D. Deposition and mechanical properties of δ-TaN_x films with different stoichiometry by DC magnetron sputtering. *Surf. Coat. Technol.* **2020**, *404*, 126452. [CrossRef]
3. Baker, C.C.; Shah, S.I. Reactive sputter deposition of tungsten nitride thin films. *J. Vac. Sci. Technol. A* **2002**, *20*, 1699–1703. [CrossRef]
4. Lou, B.S.; Moirangthem, I.; Lee, J.W. Fabrication of tungsten nitride thin films by superimposed HiPIMS and MF system: Effects of nitrogen flow rate. *Surf. Coat. Technol.* **2020**, *393*, 125743. [CrossRef]
5. Inspektor, A.; Salvador, P.A. Architecture of PVD coatings for metalcutting applications: A review. *Surf. Coat. Technol.* **2014**, *257*, 138–153. [CrossRef]
6. Nordin, M.; Ericson, F. Growth characteristics of multilayered physical vapour deposited TiN/TaN_x on high speed steel substrate. *Thin Solid Films* **2001**, *385*, 174–181. [CrossRef]
7. Chen, Y.I.; Lin, B.L.; Kuo, Y.C.; Huang, J.C.; Chang, L.C.; Lin, Y.T. Preparation and annealing study of TaN_x coatings on WC-Co substrates. *Appl. Surf. Sci.* **2011**, *257*, 6741–6749. [CrossRef]
8. Riekkinen, T.; Molarius, J.; Laurila, T.; Nurmela, A.; Suni, I.; Kivilahti, J.K. Reactive sputter deposition and properties of Ta_xN thin films. *Microelectron. Eng.* **2002**, *64*, 289–297. [CrossRef]
9. Dalili, N.; Liu, Q.; Ivey, D.G. Thermal and electrical stability of TaN_x diffusion barriers for Cu metallization. *J. Mater. Sci.* **2013**, *48*, 489–501. [CrossRef]
10. Leng, Y.X.; Sun, H.; Yang, P.; Chen, J.Y.; Wang, J.; Wan, G.J.; Huang, N.; Tian, X.B.; Wang, L.P.; Chu, P.K. Biomedical properties of tantalum nitride films synthesized by reactive magnetron sputtering. *Thin Solid Films* **2001**, *398–399*, 471–475. [CrossRef]
11. Jiang, P.C.; Chen, J.S.; Lin, Y.K. Structural and electrical characteristics of W–N thin films prepared by reactive rf sputtering. *J. Vac. Sci. Technol. A* **2003**, *21*, 616–622. [CrossRef]
12. Lee, G.R.; Lee, J.J.; Shin, C.S.; Petrov, I.; Greene, J.E. Self-organized lamellar structured tantalum–nitride by UHV unbalanced-magnetron sputtering. *Thin Solid Films* **2005**, *475*, 45–48. [CrossRef]
13. Li, T.C.; Lwo, B.J.; Pu, N.W.; Yu, S.P.; Kao, C.H. The effects of nitrogen partial pressure on the properties of the TaN_x films deposited by reactive magnetron sputtering. *Surf. Coat. Technol.* **2006**, *201*, 1031–1036. [CrossRef]
14. Bernoulli, D.; Müller, U.; Schwarzenberger, M.; Hauert, R.; Spolenak, R. Magnetron sputter deposited tantalum and tantalum nitride thin films: An analysis of phase, hardness and composition. *Thin Solid Films* **2013**, *548*, 157–161. [CrossRef]
15. Yang, Y.H.; Chen, D.J.; Wu, F.B. Microstructure, hardness, and wear resistance of sputtering TaN coating by controlling RF input power. *Surf. Coat. Technol.* **2016**, *303*, 32–40. [CrossRef]
16. Chim, Y.C.; Ding, X.Z.; Zeng, X.T.; Zhang, S. Oxidation resistance of TiN, CrN, TiAlN and CrAlN coatings deposited by lateral rotating cathode arc. *Thin Solid Films* **2009**, *517*, 4845–4849. [CrossRef]
17. Tang, J.F.; Lin, C.Y.; Yang, F.C.; Chang, C.L. Influence of nitrogen content and bias voltage on residual stress and the tribological and mechanical properties of CrAlN films. *Coatings* **2020**, *10*, 546. [CrossRef]
18. Lin, C.H.; Duh, J.G.; Yau, B.S. Processing of chromium tungsten nitride hard coatings for glass molding. *Surf. Coat. Technol.* **2006**, *201*, 1316–1322. [CrossRef]
19. Huang, A.; Xie, Z.; Li, K.; Chen, Q.; Chen, Y.; Gong, F. Thermal stability of CrWN glass molding coatings after vacuum annealing. *Coatings* **2020**, *10*, 198. [CrossRef]
20. Chang, L.C.; Chang, C.Y.; Chen, Y.I. Mechanical properties and oxidation resistance of reactively sputtered $Ta_{1-x}Zr_xN_y$ thin films. *Surf. Coat. Technol.* **2015**, *280*, 27–36. [CrossRef]
21. Wei, C.T.; Shieh, H.P.D. Effects of processing variables on tantalum nitride by reactive-ion-assisted magnetron sputtering deposition. *Jpn. J. Appl. Phys.* **2006**, *45*, 6405–6410. [CrossRef]
22. Hones, P.; Sanjinés, R.; Lévy, F. Sputter deposited chromium nitride based ternary compounds for hard coatings. *Thin Solid Films* **1998**, *332*, 240–246. [CrossRef]
23. Čekada, M.; Panjan, P.; Navinšek, B.; Cvelbar, F. Characterization of (Cr,Ta)N hard coatings reactively sputtered at low temperature. *Vacuum* **1999**, *52*, 461–467. [CrossRef]
24. Zhao, X.; Li, H.; Li, J.; Hu, J.; Huang, J.; Kong, J.; Wu, Q.; Shi, Y.; Xiong, D. Mechanical and tribological behaviors of hard and tough $Ta_xHf_{1-x}N$ films with various Ta contents. *Surf. Coat. Technol.* **2020**, *403*, 126412. [CrossRef]
25. Xu, J.; Xue, Y.; Cao, J.; Yu, L. Microstructures, Mechanical and Friction Properties of TaMoN Composite Films. *Rare Metal Mater. Eng.* **2014**, *43*, 1412–1416.

26. Yang, J.F.; Jiang, Y.; Yuan, Z.G.; Wang, X.P.; Fang, Q.F. Manufacture, microstructure and mechanical properties of W–Ta–N nano-structured hard films. *Appl. Surf. Sci.* **2012**, *258*, 7849–7854. [CrossRef]
27. Xu, J.; Luo, H.; Ju, H.; Yu, L.; Zhou, G. Microstructure, mechanical and tribological properties of TaWN composite films. *Vacuum* **2017**, *146*, 246–251. [CrossRef]
28. Liu, Y.; Song, S.; Mao, D.; Ling, H.; Li, M. Diffusion barrier performance of reactively sputtered Ta–W–N between Cu and Si. *Microelectron. Eng.* **2004**, *75*, 309–315. [CrossRef]
29. Takeyama, M.B.; Sato, M.; Yasuda, M. Relationship between ⟨111⟩-oriented Cu film and thin Ta–W–N barrier. *Jpn. J. Appl. Phys.* **2020**, *59*, SLLD02. [CrossRef]
30. Chang, L.C.; Zheng, Y.Z.; Gao, Y.X.; Chen, Y.I. Mechanical properties and oxidation resistance of sputtered Cr–W–N coatings. *Surf. Coat. Technol.* **2017**, *320*, 196–200. [CrossRef]
31. Yang, J.F.; Yuan, Z.G.; Wang, X.P.; Fang, Q.F. Characterization of W–Ta–N hard films synthesized by direct current magnetron sputtering. *Surf. Coat. Technol.* **2013**, *231*, 19–23. [CrossRef]
32. Chen, Y.I.; Lin, K.Y.; Wang, H.H.; Cheng, Y.R. Characterization of Ta–Si–N coatings prepared using direct current magnetron co-sputtering. *Appl. Surf. Sci.* **2014**, *305*, 805–816. [CrossRef]
33. Tong, C.Y.; Lee, J.W.; Kuo, C.C.; Huang, S.H.; Chan, Y.C.; Chen, H.W.; Duh, J.G. Effects of carbon content on the microstructure and mechanical property of cathodic arc evaporation deposited CrCN thin films. *Surf. Coat. Technol.* **2013**, *231*, 482–486. [CrossRef]
34. Cullity, B.D.; Stock, S.R. *Elements of X-ray Diffraction*, 3rd ed.; Prentice-Hall: Hoboken, NJ, USA, 2001; pp. 169–170.
35. Greczynski, G.; Hultman, L. C1s peak of adventitious carbon aligns to the vacuum level: Dire consequences for material's bonding assignment by photoelectron spectroscopy. *Chem. Phys. Chem.* **2017**, *18*, 1507–1512. [CrossRef]
36. Greczynski, G.; Hultman, L. Reliable determination of chemical state in X-ray photoelectron spectroscopy based on sample-work-function referencing to adventitious carbon: Resolving the myth of apparent constant binding energy of the C 1s peak. *Appl. Surf. Sci.* **2018**, *451*, 99–103. [CrossRef]
37. Moulder, J.F.; Stickle, W.F.; Sobol, P.E.; Bomben, K.D. *Handbook of X-ray Photoelectron Spectroscopy*; Chastain, J., King, R.C., Eds.; Physical Electronics: Chanhassen, MN, USA, 1995.
38. Oliver, W.C.; Pharr, G.M. An improved technique for determining hardness and elastic modulus using load and displacement sensing indentation experiments. *J. Mater. Res.* **1992**, *7*, 1564–1583. [CrossRef]
39. Janssen, G.C.A.M.; Abdalla, M.M.; van Keulen, F.; Pujada, B.R.; van Venrooy, B. Celebrating the 100th anniversary of the Stoney equation for film stress: Developments from polycrystalline steel strips to single crystal silicon wafers. *Thin Solid Films* **2009**, *517*, 1858–1867. [CrossRef]
40. Thod, L.E. *Transition Metal Carbides and Nitrides*; Academic Press: New York, NY, USA, 1971.
41. Barin, I. *Thermochemical Data of Pure Substances*, 3rd ed.; VCH: New York, NY, USA, 1995.
42. de Boer, F.R.; Boom, R.; Mattens, W.C.M.; Miedema, A.R.; Niessen, A.K. *Transition Metal Alloys*; North-Holland: Amsterdam, The Netherlands, 1988.
43. Senkov, O.N.; Miracle, D.B. Effect of the atomic size distribution on glass forming ability of amorphous metallic alloys. *Mater. Res. Bull.* **2001**, *36*, 2183–2198. [CrossRef]
44. Chang, C.C.; Jeng, J.S.; Chen, J.S. Microstructural and electrical characteristics of reactively sputtered Ta-N thin films. *Thin Solid Films* **2002**, *413*, 46–51. [CrossRef]
45. Arranz, A.; Palacio, C. Composition of tantalum nitride thin films grown by low-energy nitrogen implantation: A factor analysis study of the Ta 4f XPS core level. *Appl. Phys. A* **2005**, *81*, 1405–1410. [CrossRef]
46. Scandurra, A.; Indelli, G.F.; Pignataro, B.; Di Marco, S.; Di Stefano, M.A.; Ravesi, S.; Pignataro, S. Tantalum nitride thin film resistors by low temperature reactive sputtering for plastic electronics. *Surf. Interface Anal.* **2008**, *40*, 758–762. [CrossRef]
47. Arshi, N.; Lu, J.; Joo, Y.K.; Yoon, J.H.; Koo, B.H. Effects of nitrogen composition on the resistivity of reactively sputtered TaN thin films. *Surf. Interface Anal.* **2015**, *47*, 154–160. [CrossRef]
48. Zaman, A.; Meletis, E.I. Microstructure and mechanical properties of TaN thin films prepared by reactive magnetron sputtering. *Coatings* **2017**, *7*, 209. [CrossRef]
49. Wen, M.; Meng, Q.N.; Yu, W.X.; Zheng, W.T.; Mao, S.X.; Hua, M.J. Growth, stress and hardness of reactively sputtered tungsten nitride thin films. *Surf. Coat. Technol.* **2010**, *205*, 1953–1961. [CrossRef]
50. Fu, T.; Shen, Y.G.; Zhou, Z.F.; Li, K.Y. Thermal stability of sputter deposited nanocrystalline W_2N/amorphous Si_3N_4 coatings. *J. Vac. Sci. Technol. A* **2006**, *24*, 2094–2099. [CrossRef]
51. Louro, C.; Cavaleiro, A.; Montemor, F. How is the chemical bonding of W–Si–N sputtered coatings? *Surf. Coat. Technol.* **2001**, *142–144*, 964–970. [CrossRef]
52. Liu, Y.H.; Chang, L.C.; Liu, B.W.; Chen, Y.I. Mechanical properties and oxidation behavior of W–Si–N coatings. *Surf. Coat. Technol.* **2019**, *375*, 727–738. [CrossRef]
53. Shen, L.; Wang, N. Effect of nitrogen pressure on the structure of Cr-N, Ta-N, Mo-N, and W-N nanocrystals synthesized by arc discharge. *J. Nanomater.* **2011**, *2011*, 781935. [CrossRef]
54. Greczynski, G.; Primetzhofer, D.; Lu, J.; Hultman, L. Core-level spectra and binding energies of transition metal nitrides by non-destructive X-ray photoelectron spectroscopy through capping layers. *Appl. Surf. Sci.* **2017**, *396*, 347–358. [CrossRef]
55. Naik, S.N.; Walley, S.M. The Hall–Petch and inverse Hall–Petch relations and the hardness of nanocrystalline metals. *J. Mater. Sci.* **2020**, *55*, 2661–2681. [CrossRef]

56. Quek, S.S.; Chooi, Z.H.; Wu, Z.; Zhang, Y.W.; Srolovitz, D.J. The inverse hall–petch relation in nanocrystalline metals: A discrete dislocation dynamics analysis. *J. Mech. Phys. Solids* **2016**, *88*, 252–266. [CrossRef]
57. Mayrhofer, P.H.; Tischler, G.; Mitterer, C. Microstructure and mechanical/thermal properties of Cr–N coatings deposited by reactive unbalanced magnetron sputtering. *Surf. Coat. Technol.* **2001**, *142–144*, 78–84. [CrossRef]
58. Escobar, D.; Ospina, R.; Gómez, A.G.; Restrepo-Parra, E. Microstructure, residual stress and hardness study of nanocrystalline titanium–zirconium nitride thin films. *Ceram. Int.* **2015**, *41*, 947–952. [CrossRef]
59. Tan, P.; Fu, L.; Teng, J.; Zhu, J.; Yang, W.; Li, D.; Zhou, L. Effect of texture on wear resistance of tantalum nitride film. *Tribo. Int.* **2019**, *133*, 126–135. [CrossRef]
60. Addonizio, M.L.; Castaldo, A.; Antonaia, A.; Gambale, E.; Iemmo, L. Influence of process parameters on properties of reactively sputtered tungsten nitride thin films. *J. Vac. Sci. Technol. A* **2012**, *30*, 031506. [CrossRef]
61. Chang, L.C.; Sung, M.C.; Chu, L.H.; Chen, Y.I. Effects of the nitrogen flow ratio and substrate bias on the mechanical properties of W–N and W–Si–N Films. *Coatings* **2020**, *10*, 1252. [CrossRef]
62. Pogrebnjak, A.D.; Beresnev, V.M.; Bondar, O.V.; Postolnyi, B.O.; Zaleski, K.; Coy, E.; Jurga, S.; Lisovenko, M.O.; Konarski, P.; Rebouta, L.; et al. Superhard CrN/MoN coatings with multilayer architecture. *Mater. Des.* **2018**, *153*, 47–59. [CrossRef]
63. Musil, J. Hard nanocomposite coatings: Thermal stability, oxidation resistance and toughness. *Surf. Coat. Technol.* **2012**, *207*, 50–65. [CrossRef]
64. Tsui, T.Y.; Pharr, G.M.; Oliver, W.C.; Bhatia, C.S.; White, R.L.; Anders, S.; Anders, A.; Brown, I.G. Nanoindentation and nanoscratching of hard carbon coatings for magnetic disks. *Mater. Res. Soc. Symp. Proc.* **1995**, *383*, 447–452. [CrossRef]
65. Chen, X.; Du, Y.; Chung, Y.W. Commentary on using H/E and H^3/E^2 as proxies for fracture toughness of hard coatings. *Thin Solid Films* **2019**, *688*, 137265. [CrossRef]
66. Kim, D.J.; La, J.H.; Kim, K.S.; Kim, S.M.; Lee, S.Y. Tribological properties of CrZr–Si–N films synthesized using Cr–Zr–Si segment targets. *Surf. Coat. Technol.* **2014**, *259*, 71–76. [CrossRef]